IEEE Access
Multidisciplinary | Rapid Review | Open Access Journal

Received 19 June 2024, accepted 19 July 2024, date of publication 24 July 2024, date of current version 2 August 2024.

Digital Object Identifier 10.1109/ACCESS.2024.3432884

RESEARCH ARTICLE

Stiffness Loss of Curvic Coupling Under Bending Vibration and Its Effect on Dynamic Characteristics of Rotor Systems

XING HENG AND AILUN WANG
School of Mechanical and Electrical Engineering, Central South University, Changsha 410083, China
State Key Laboratory of Precision Manufacturing for Extreme Service Performance, Changsha 410083, China

Corresponding author: Ailun Wang (193701033@csu.edu.cn)

This work was supported in part by the National Natural Science Foundation of China under Grant 52075554, and in part by the State Key Laboratory of Precision Manufacturing for Extreme Service Performance Foundation Project under Grant ZZYJKT2021-07.

ABSTRACT Aiming at the complex mechanical characteristics of the curvic coupling in the aero-engine rotor under operation condition, the contact stiffness model of the curvic coupling under the bending vibration is proposed to study the law of stiffness loss of the curvic coupling and the dynamic characteristics of the rotor with the curvic coupling under the bending vibration. Based on the Hertz contact theory and the elastic-plastic contact theory, an analytical model for the contact stiffness of the three-dimensional curvic coupling is established considering the complex geometric characteristics of the curvic coupling. And the law of stiffness loss of the curvic coupling under the bending vibration is studied. Then, a finite element model of the rotor system is proposed and the dynamic characteristics of the rotor system is analyzed. The results are tested and verified. The results show that the stiffness loss of the curvic coupling under the bending vibration is increased and the critical speed of the rotor is decreased caused by the increased stiffness loss. The contact stiffness model and research conclusions proposed in this paper provide an important theoretical basis for the design and dynamic characteristics analysis of modern aero-engine rotor systems.

INDEX TERMS Aero-engine rotor, curvic coupling, bending vibration, stiffness loss, contact stiffness model, dynamic characteristics.

I. INTRODUCTION

For the convenience of installation and maintenance, and the lightweight of the structure, the majority of modern aero-engine rotor systems are designed with non-continuous rotor systems. Due to the advantages of strong transmission capability, automatic centering, high strength, and high precision, a curvic coupling is the main connecting structure for the non-continuous rotors in modern aero-engines.

In the early research on the dynamic characteristics of rotor systems with a the curvic coupling, the influence of stiffness loss of non-continuous rotors was often not considered [1].

With the improvement in design requirements for modern aero-engines, the accuracy of the model of aero-engine rotors are also need to be increased. Scholars have studied the impact of the stiffness loss of curvic coupling joints on the vibration characteristics of rotors from both theoretical and experimental perspectives. The research results indicate that the influence of contact stiffness on the transient characteristics [2], critical speeds [3], and vibration modes [4] of rotors cannot be ignored. Therefore, when analyzing the dynamic characteristics of aero-engine rotor systems, it is necessary to consider the influence of the contact stiffness of the curvic coupling.

In order to investigate the mechanism of how the contact stiffness of curvic coupling affects the vibration characteristics of the rotor, Scholars have conducted a series of research works on the contact stiffness of a curvic coupling based on theories such as elastoplasticity, interface mechanics, and tribology. Rao et al. [5] studied the influence of surface waviness on the contact stiffness of the contact plane based on the GW model. Zhang et al. [6] and Shi and Zhang [7], [8]

The associate editor coordinating the review of this manuscript and approving it for publication was Zhenbao Liu.

respectively studied the effects of the axial preload force and the roughness of the contact surface on the contact stiffness of tie-rod rotors. Yuan et al. [9], [10] used the equivalent spring method to study the variation law of contact stiffness with axial pressure and the variation law of equivalent bending stiffness of a curvic coupling with the preload force and the contact area.

In addition, Considering that operating conditions and loads can affect the stiffness of the curvic coupling by changing the contact conditions of the contact surface, scholars have studied the effects of static bending deformation and moments on planar contact stiffness [11], [12], and analyzed the vibration characteristics of discontinuous beams with a curvic coupling under bending vibration [13]. The research results indicate that bending deformation and moments can affect the contact stiffness of end teeth and the vibration characteristics of discontinuous beams with a curvic coupling.

In summary, scholars have conducted in-depth research on the variation law and influencing mechanisms of the stiffness loss of the curvic coupling under static conditions.

For the aero-engine rotors, the bending vibration of rotors is present during operation due to the residual unbalance mass. And the dynamic bending deformations and moments caused by the bending vibration can affect the stress of the curvic coupling [14]. Moreover, the curvic coupling in the aero-engine rotor have complex geometric features.

Because of the fact that existing studies mainly focus on the curvic coupling under static conditions and simplify the curvic coupling into a simple planar form, it is evident that the existing research results are not fully applicable to the curvic coupling with complex geometric features in the aero-engine rotor under operation.

Therefore, it is necessary to analyze the contact stiffness of the curvic coupling in the aero-engine rotor under the bending vibration. However, there are currently no reports on rotors with a curvic coupling under the bending vibration.

This paper firstly to presents a mechanical model of the curvic coupling considering the geometric characteristics, and then establishes a contact stiffness model under bending vibration effects, subsequently, the variation law of the stiffness loss under the bending vibration are analyzed, finally, the study investigates the impact of stiffness loss in combined rotors with circular fillet teeth under bending vibration conditions on rotor vibration characteristics. The research results can provide theoretical basis for the design and analysis of modern aero-engine rotor, such as the establishment of a more accurate analysis model for high speed rotors and even ultra-high speed rotors.

II. THE THREE-DIMENSIONAL MECHANICAL MODEL OF THE CURVIC COUPLING UNDER THE BENDING VIBRATION

As shown in Figure 1, the curvic coupling is a structure with central symmetry, so the modeling method for the single teeth of a curvic coupling can be used to establish the model of the tooth in other positions. Therefore, in this section,

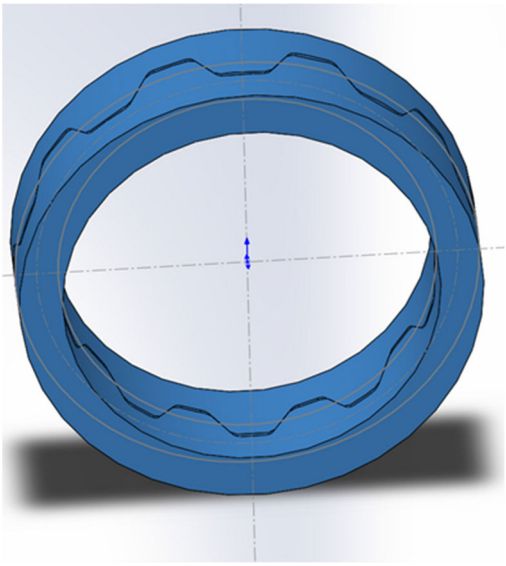

FIGURE 1. The structure of the curvic coupling.

the mechanics model of the single tooth with the three-dimensional geometric features is established, and then the mechanical model of the curvic coupling under bending vibration can be provided.

The mechanical model of the single teeth $ABCDD_1C_1B_2A_2$ under bending vibration is as shown in Figure 2.

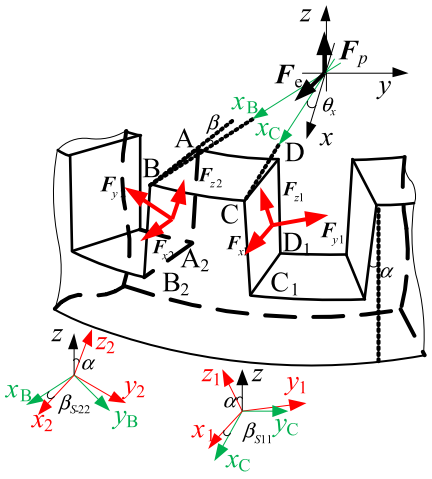

FIGURE 2. The mechanics model of the single tooth with the three-dimensional geometric features.

In the diagram, A, B, C, D, D_1, C_1, B_2, and A_2 represent the geometric boundary points of the contact surfaces; CDD_1C_1 is the contact surface 1 of the single tooth; ABB_2A_2 is the contact surface 2 of the single tooth and; x-y-z is the absolute coordinate system; x_B-y_B-z and x_C-y_C-z are the relative coordinate systems established based on the entry points B and C which are the starting points during Grinding processing, which is marked in green; x_1-y_1-z_1 and x_2-y_2-z_2 are the relative coordinate systems established based on the contact surfaces CDD_1C_1 and ABB_2A_2 respectively, which is

marked in red; $\boldsymbol{F}_{\mathrm{e}}$ and $\boldsymbol{F}_{\mathrm{p}}$ represent the unbalance force, and the preload force acting on the curvic coupling, respectively; $\boldsymbol{F}_x$, $\boldsymbol{F}_y$, and $\boldsymbol{F}_z$ represent the components of the contact force on the contact surface of the tooth, where $\boldsymbol{F}_x$ and $\boldsymbol{F}_z$ are tangential forces, and $\boldsymbol{F}_y$ is the normal force. α and β are the angles which are able to characterize the geometric features of the contact surface.

Based on Figure 2, the mechanical equation for a single teeth is:

$$\begin{cases} \boldsymbol{F}_e + \boldsymbol{F}_p + \sum_{i=1}^{2} (F_{xi} + F_{yi} + F_{zi}) = 0 \\ \boldsymbol{F}_e \cdot z_e = \sum_{i=1}^{2} (F_{xi} + F_{yi} + F_{zi}) \cdot x_i \end{cases} \tag{1}$$

where

$$\boldsymbol{F}_e = \begin{bmatrix} f_{ex} \\ f_{ey} \\ 0 \end{bmatrix}, \quad \boldsymbol{F}_p = \begin{bmatrix} 0 \\ 0 \\ f_p \end{bmatrix}, \quad \boldsymbol{F}_{xi} = \begin{bmatrix} f_{xi} \\ 0 \\ 0 \end{bmatrix},$$
$$\boldsymbol{F}_{yi} = \begin{bmatrix} 0 \\ f_{yi} \\ 0 \end{bmatrix}, \quad \boldsymbol{F}_{zi} = \begin{bmatrix} 0 \\ 0 \\ f_{zi} \end{bmatrix}$$

In (1), $\boldsymbol{F}_e$, $\boldsymbol{F}_p$, and $\boldsymbol{F}_T$ are vectors in the absolute coordinate system x-y-z, and the contact force components $\boldsymbol{F}_x$, $\boldsymbol{F}_y$, and $\boldsymbol{F}_z$ are vectors in the relative coordinate system x_1-y_1-z_1 and x_2-y_2-z_2. According to the coordinate transformation relationship, Equation (1) can be rewritten as:

$$\begin{cases} \boldsymbol{F}_e + \boldsymbol{F}_p = \sum_{i=1}^{2} [\boldsymbol{S}_{ii} S_i (F_{xi} + F_{yi} + F_{zi})] \\ \boldsymbol{F}_e \cdot z_e = \sum_{i=1}^{2} [\boldsymbol{S}_{ii} S_i (F_{xi} + F_{yi} + F_{zi})] \cdot x_i \end{cases} \tag{2}$$

where, $\boldsymbol{S}_i$ (i = 1,2) represents the coordinate transformation matrix between x-y-z with x_B-y_B-z and x_C-y_C-z; $\boldsymbol{S}_{ii}$ (i = 1,2) is the coordinate transformation matrix between x_i-y_i-z_i with x_B-y_B-z and x_C-y_C-z.

The coordinate rotation angle β_{Si} (i = 1,2) of the coordinate transformation matrix $\boldsymbol{S}_i$ can be calculated as follows:

$$\beta_{Si} = \frac{\pi}{2Z} + (-1)^{i-1} \frac{\pi}{2Z} - \theta_x \tag{3}$$

The coordinate rotation angle of the coordinate transformation matrix $\boldsymbol{S}_{ii}$ is α and β_{Sii}. And β_{Sii} (i = 1,2) can be expressed as:

$$\beta_{Sii} = (-1)^{i-1} \beta \tag{4}$$

According to the machining process of the curvic coupling in areo-engine rotors shown in Figure 3, α is 30°, and the formula of β can be derived as follows:

$$\begin{aligned} \angle\beta &= \angle \mathrm{o_1AB} \\ &= \arccos \frac{R_m^2 + R_o^2 - S^2}{2R_m R_o} + \frac{1}{2} \arccos \frac{R_m^2 + S^2 - R_o^2}{2R_m S} \\ &\quad - \frac{1}{2} \arccos \frac{R_m^2 + S^2 - R_i^2}{2R_m S} - \frac{\pi}{2} \end{aligned} \tag{5}$$

Where R_i and R_o are the inner and outer radius, $R_i = 0.5D_i$, $R_o = 0.5D_o$; N_X is the number between two tooth surfaces machined in a single operation; Z is the number of teeth; R_m is the grinding wheel inner diameter, $R_m = 0.5(R_i + R_o)\tan\theta$; $\theta = 0.5\pi \times N_X/Z$; S is the distance from $\mathrm{o_1}$ to $\mathrm{o_2}$, $S = R_m/\sin\theta$.

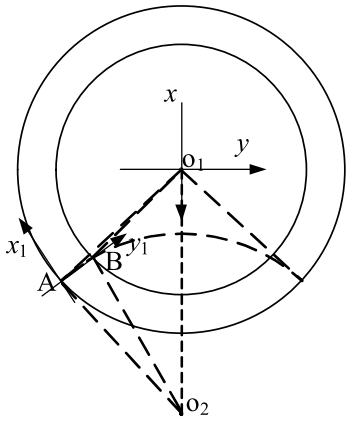

FIGURE 3. The grinding process diagram of the curvic coupling.

According to Eq.(5), the variation law of β with the changes in the machining parameters N_X and Z, as shown in Figure 4.

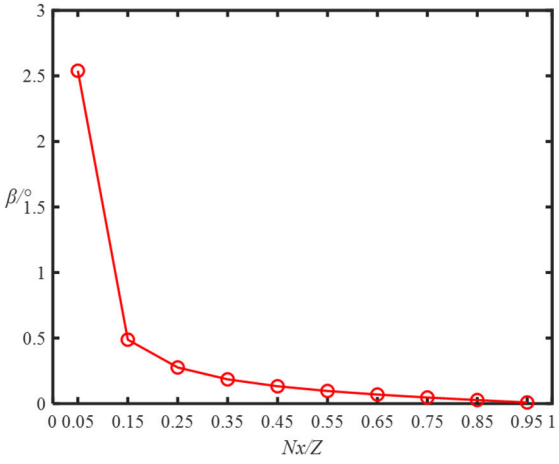

FIGURE 4. The grinding process diagram of the curvic coupling.

The curve in Figure 4 is a discrete plot for the reason that the values of Z can only be integers and the values of N_X is an odd number ranging from 1 to Z. Based on Figures 4, it can be observed that the angle β is positively correlated with N_X and negatively correlated with the number of teeth Z. When $N_X/Z > 0.25$, $\beta < 0.5°$, the angle β approaches 0.

III. MODELING OF CONTACT STIFFNESS OF THE CURVIC COUPLING UNDER BENDING VIBRATION

While rotors operating, the curvic coupling under bending vibration simultaneously undergoes rotational motion around the axis and lateral bending vibration. According to the dynamic characteristic of rotor shown, the phase difference

between the rotational period and the vibration period and the direction of the bending moment caused by the unbalanced force remain constant, and the direction of the unbalanced force passes through both the balanced position and the axis of the curvic coupling simultaneously.

Due to the small amplitude of the rotor system of aircraft engines, the stress on the contact surface of the curvic coupling exhibits a linear distribution characteristic [11]. Therefore, a linear function $p(x)$ can be used to represent the stress distribution in the z-axis direction on the contact surface:

$$p(x) = ax + b \tag{6}$$

The parameters a and b in the Eq.(6) can be calculated by the preload force F_p and bending moment M.

$$\begin{cases} F_p = \iint_A p(x)dA = aS_y + bA \\ M = \iint_A p(x)xdA = aI_y + bS_y \end{cases} \tag{7}$$

where A represents the contact area; S_y and I_y are the static moment and inertia moment of the curvic coupling; $M = F_{\mathrm{p}} \cdot z$.

Based on Eq.(7), the function of $p(x)$ is:

$$p(x) = p_{Fp} - p_M(x) \tag{8}$$

where

$$p_{Fp} = \frac{F_p}{A}, \quad p_M(x) = \frac{M - \frac{F_p}{A}S_y}{AI_y - S_y^2}(S_x - Ax).$$

Then, In Eq.(8), S_y and I_y can be represented as:

$$\begin{cases} S_y = \sum_{j=1}^{Z} (\iint_{\mathrm{A_{j1}}} x_{1i} \cdot d\mathrm{A_{j1}} + \iint_{\mathrm{A_{j2}}} x_{2i} \cdot d\mathrm{A_{j2}}) \\ I_y = \sum_{j=1}^{Z} (\iint_{\mathrm{A_{j1}}} x_{1i}^2 \cdot d\mathrm{A_{j1}} + \iint_{\mathrm{A_{j2}}} x_{2i}^2 \cdot d\mathrm{A_{j2}}) \end{cases} \tag{9}$$

where x_{1i} represents the x-axis coordinate of any point on surface $\mathrm{CDD_1C_1}$; x_{2i} represents the x-axis coordinate of any point on surface $\mathrm{ABB_2A_2}$; $\mathrm{A_{j1}}$ represents the contact surface area of surface $\mathrm{CDD_1C_1}$; $\mathrm{A_{j2}}$ represents the contact surface area of surface $\mathrm{ABB_2A_2}$.

The coordinates on the x and y axes of the geometric boundary points A, B, C, D, $\mathrm{A_2}$, $\mathrm{B_2}$, $\mathrm{C_1}$ and $\mathrm{D_1}$ can be determined, by geometric relationships shown in Figure 5. The coordinates is as follows:

$$\begin{aligned}
x_{\mathrm{A}} &= R_{\mathrm{i}} \cos(-\theta_x - \theta_1 + \theta_2), \; y_{\mathrm{A}} = R_{\mathrm{i}} \sin(-\theta_x - \theta_1 + \theta_2), \\
x_{\mathrm{B}} &= R_o \cos(-\theta_x - \theta_1), \; y_{\mathrm{B}} = R_o \sin(-\theta_x - \theta_1), \\
x_{\mathrm{C}} &= R_o \cos(-\theta_x), \; y_{\mathrm{C}} = R_o \sin(-\theta_x), \\
x_{\mathrm{D}} &= R_o \cos(-\theta_x - \theta_2), \; y_{\mathrm{D}} = R_o \sin(-\theta_x - \theta_2), \\
x_{\mathrm{A_2}} &= R_{\mathrm{i}} \cos\left(-\theta_x - \theta_1 + \theta_2 - \theta_{\mathrm{AA_2}}\right), \\
y_{\mathrm{A_2}} &= R_{\mathrm{i}} \sin\left(-\theta_x - \theta_1 + \theta_2 - \theta_{\mathrm{AA_2}}\right), \\
x_{\mathrm{B_2}} &= R_o \cos\left(-\theta_x - \theta_1 - \theta_{\mathrm{BB_2}}\right), \\
y_{\mathrm{B_2}} &= R_o \sin\left(-\theta_x - \theta_1 - \theta_{\mathrm{BB_2}}\right), \\
x_{\mathrm{C_1}} &= R_o \cos\left(-\theta_x + \theta_{\mathrm{BB_2}}\right), \; y_{\mathrm{C_1}} = R_o \sin\left(-\theta_x + \theta_{\mathrm{BB_2}}\right), \\
x_{\mathrm{D_1}} &= R_o \cos\left(-\theta_x - \theta_2 + \theta_{\mathrm{AA_2}}\right), \\
y_{\mathrm{D_1}} &= R_o \sin\left(-\theta_x - \theta_2 + \theta_{\mathrm{AA_2}}\right).
\end{aligned}$$

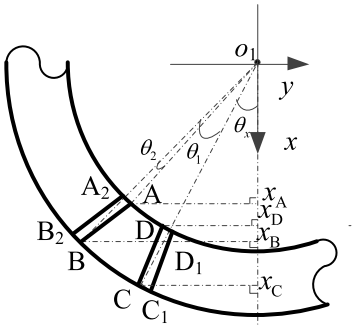

FIGURE 5. The projection of the contact surface on the x-y plane.

According to geometric relationships shown in Figure 6, It is easy to calculate the angular parameters of the above coordinates. The parameters is as follows:

$$\theta_1 = \frac{\widehat{l}_{\mathrm{BC}}}{R_{\mathrm{o}}}, \quad \theta_{\mathrm{BB_2}} = \theta_{\mathrm{CC_1}} = \frac{\widehat{l}_{\mathrm{BB_2}}}{R_{\mathrm{o}}}, \; \theta_{\mathrm{AA_2}} = \theta_{\mathrm{DD_1}} = \frac{\widehat{l}_{\mathrm{AA_2}}}{R_{\mathrm{i}}},$$

$$\theta_2 = \arccos\frac{S^2 + R_{\mathrm{o}}^2 - R_m^2}{2SR_{\mathrm{o}}} - \arccos\frac{S^2 + R_{\mathrm{i}}^2 - R_m^2}{2SR_{\mathrm{i}}}.$$

Based on the above analysis, the component force on the surface contact force in the z-axis direction can be determined:

$$\begin{cases} f_{Z1} = \iint_{\mathrm{A1}} p(x_{1i})d\mathrm{A}_{1i} \\ f_{Z2} = \iint_{\mathrm{A2}} p(x_{2i}) \cdot d\mathrm{A}_{2i} \end{cases} \tag{10}$$

Then, the contact force *fni* on the any contact surface of the curvic coupling can be established:

$$\begin{cases} \boldsymbol{f}_{n1} = \boldsymbol{S}_{-1} \iint_{\mathrm{A}_{n1}} p(x_{1i})d\mathrm{A}_{n1} \\ \boldsymbol{f}_{n2} = \boldsymbol{S}_{-1} \iint_{\mathrm{A}_{n2}} p(x_{2i})d\mathrm{A}_{n2} \end{cases} \tag{11}$$

where S_{-1} is the relationship matrix between f_{Zi} and f_{ni} which can be derived by the matrix $\boldsymbol{S}_{ij}$

According to Hertz contact theory and the elastic-plastic contact theory, the contact stiffness of rough surfaces is [15]:

$$k_n = \frac{f_n}{\sigma} \tag{12}$$

where σ represents the standard deviation of the asperity of rough surfaces; and f_n represents the contact force and is the equation of the elastic-plastic contact of the asperity of rough surfaces.

Subsequently, the contact stiffness of any contact surface k_{ni} is of the curvic coupling:

$$k_{ni} = \frac{\boldsymbol{S}_{-1} \iint_{\mathrm{A}_{nj}} p(x_{ji})d\mathrm{A}_{nj}}{\sigma}, j = 1, 2 \tag{13}$$

Therefore, the contact stiffness of the curvic coupling KN is:

$$K_N = \sum_{n=1}^{Z} \frac{\boldsymbol{S}_{-1} \iint_{\mathrm{A}_{nj}} p(x_{ji}) d\mathrm{A}_{nj}}{\sigma} \tag{14}$$

According to Eq.(8), The Eq.(14) can be rewritten as:

$$K_N = K_{Fp} - K_M \tag{15}$$

where

$$K_{Fp} = \sum_{n=1}^{Z} \frac{\boldsymbol{S}_{-1} \iint_{\mathrm{A}_{nj}} p_{Fp} d\mathrm{A}_{nj}}{\sigma},$$

$$K_M = \sum_{n=1}^{Z} \frac{\boldsymbol{S}_{-1} \iint_{\mathrm{A}_{nj}} p_M(x_{ji}) d\mathrm{A}_{nj}}{\sigma}$$

When $M = 0$, (13) and (14) can be simplified as and $k_{ni} = F_p/(Z\sigma)$ and $K_N = F_p/\sigma$. In conclusion, the contact stiffness of the curvic coupling under bending vibration is more universal. In conclusion, the contact stiffness under static conditions is a special case of that under bending vibration.

IV. ANALYSIS OF THE VARIATION LAW OF CONTACT STIFFNESS OF THE CURVIC COUPLING UNDER BENDING VIBRATION

According to the parameter of the curvic coupling CC1054 in the industry standard HB7808-2006, which is shown in Table 1.

TABLE 1. The parameter of the curvic coupling CC1054.

Name of Parameter	Value	Name of Parameter	Value
Poisson's ratio	0.3	The outer diameters	74 mm
The number of tooth	24	Elastic Modulus	203 Gpa
The inner diameter	55 mm	Density	8240 kg/m^3

The contact stiffness of the curvic coupling CC1054 is established, and the variation law of contact stiffness is studied. The analysis results are as shown in the following text.

The circular-arc tooth CC1054 has 24 teeth and 48 contact surfaces. All contact surfaces are numbered from 1 to 48, θ_x of surface 1 is 0. The contact stiffness of different contact surfaces k_{ni} is shown in Figure 6.

In Figure 6, when $M = 0$, the contact stiffness of each contact surface is the same; When $M > 0$, the contact stiffness of the contact surfaces in different positions is not the same, and the variation patterns are different. The contact stiffnesses on surfaces 1 to 12 are increased, and those on surfaces 13 to 35 are decreased, and those on 36 to 48 are increased. The contact stiffness on the surface 25 is the smallest. The reason is the contact force of the contact surface of a curvic coupling is changed by the bending moment. The contact force of the surface 25 is reduced the most with the increase of bending mement.

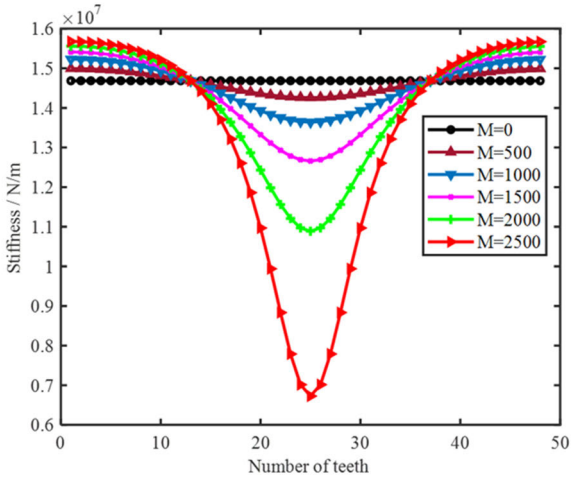

FIGURE 6. F_p = 160kN, the contact stiffness of individual contact surfaces of the curvic coupling k_{ni} under different bending moments.

When M<500 N·m, the increase in the contact stiffness is equal to the decrease in the contact stiffness. As the bending moment increases, the increase in the contact stiffness becomes smaller than the decrease in the contact stiffness. As the moment becomes larger, the difference between the increase value and the increase value increases becomes larger.

To ensure the safety of the curvic coupling, the contact surface must maintain contact at all times without separating while the rotor is operating [13]. Based on the analysis results in Figure 6, as the bending moment increases, the contact stiffness on the surface 25 decreases to 0 at first. For avoiding the separating of the contact surface. The effect of the bending moment on the contact force of the surfaces 25 is analyzed. The results are shown in Figure 7.

The maximum bending moment under which the separation of contact surfaces does not occur is influenced by $\theta_x(\theta_x \in [0, \pi/Z])$, θ_x is the angle between the surface position and the unbalance position. As shown in Figure 7(a), when the value of the bending moment is less than 1.74% of the value of the preloading force, the minimum contact force on the contact surfaces is greater than 0, ensuring that the tooth surfaces remain in contact and do not separate. For the curvic coupling CC1054, the variation in the maximum bending moment influenced by θ_x is 0.5%. When $F_p = 160$ kN, the maximum bending moment is 2784 N·mm, as shown in Figure 7(b).

Then, the influence of bending moment on the contact stiffness of the curvic coupling. The results are shown in Figure 8 and Figure 9.

As shown in Figure 8, the contact stiffness of the curvic coupling is increased with the increase in the preload force $\boldsymbol{F}_p$. When $\boldsymbol{F}_p < 80$ kN, the larger the bending moment is, the smaller the contact stiffness of the curvic coupling is. The contact stiffness is affected significantly by the

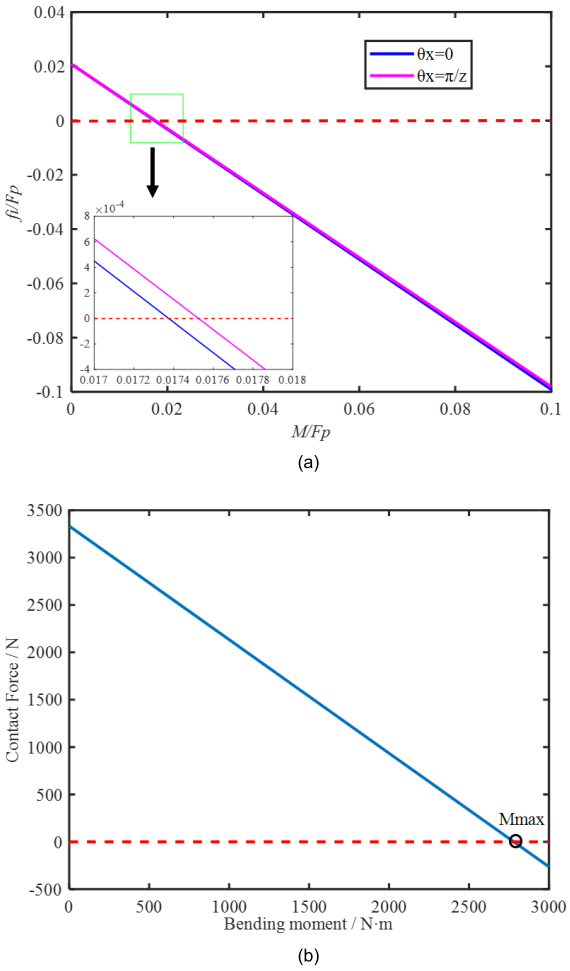

FIGURE 7. The smallest contact force of a curvic coupling under different bending moments. (a) The contact force on the surface 25 under different bending moments. (b) F_p = 160 kN, The contact force on the surface 25 under different bending moments.

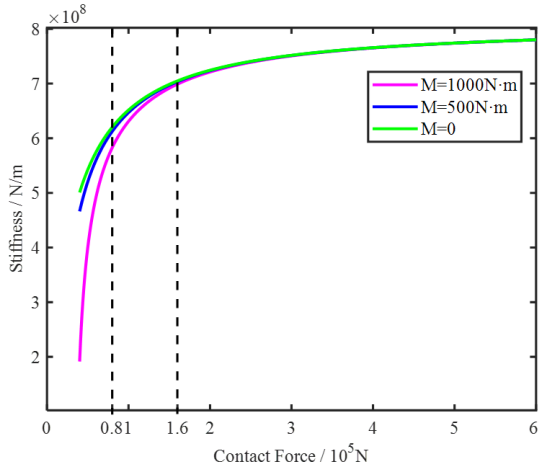

FIGURE 8. The contact stiffness of the curvic coupling under different bending moments K_N varies with the preload force.

bending moment. When 80 kN $< F_p <$ 160 kN, the bending moment from 0 to 500N·m has almost no effect on the contact stiffness, and the contact stiffness is affected significantly under the bending moment 1000 N·m. When $F_p >$ 160kN, the bending moment from 0 to 1000 N·m has almost no effect on the contact stiffness.

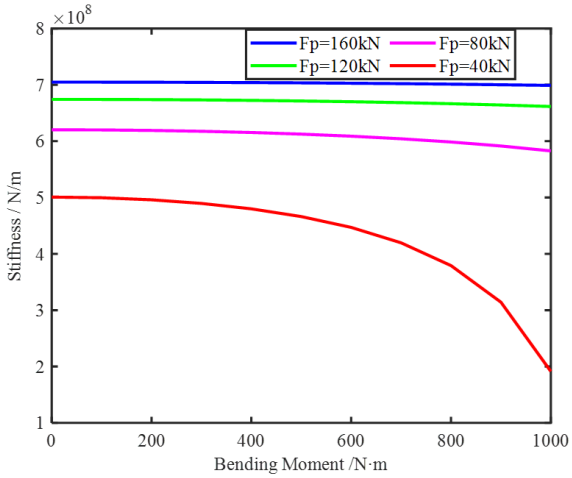

FIGURE 9. The contact stiffness of the curvic coupling under four different preload forces K_N varies with the bending moments.

In Figure 9, the curves showing the variation of contact stiffness with increasing bending moment are plotted when preloading forces is 40kN, 80kN, 120kN and 160kN. As the bending moment increases, the contact stiffness of the curvic coupling decreases. And when the bending moment is the same, the lower the preload force, the more the decrease in the contact stiffness.

In summary, the contact stiffness of the curvic coupling under working conditions is not only affected by the preload force but also by the bending moment generated by the imbalance. The bending moment causes the contact forces on the various contact surfaces of the tooth of the curvic coupling under to be no longer equal; the contact force on half of the tooth surfaces is increased while the contact force on half of the tooth surfaces is decreased. Due to the elastic-plastic contact characteristics, the increase in contact stiffness is less than the decrease in contact stiffness, which results in the decrease in the contact stiffness of the curvic coupling under the bending moment. When the preload force remains constant, the larger the bending moment, the greater the decrease in the contact stiffness. When the bending moment remains constant, the smaller preload forces, the more significant the influence of the bending moment on the contact stiffness.

V. ANALYSIS OF THE VIBRATION CHARACTERISTICS OF THE ROTORS WITH A CURVIC COUPLING

Considering the stiffness loss of the curvic coupling caused by the bending vibration, the vibration characteristics of the rotors with the curvic coupling is analyzed by the the simulation, and the results is verified by the experiment in this section.

A. SIMULATION ANALYSIS

The real rotor shown in Figure 10 is fastened by 8 rods and 4 curvic couplings, The rotor structural parameters of rotors

can be found in Table 2, and parameters of the preload force on the curvic coupling can be found in Table 3.

Based on the physical model of the rotor with a curvic coupling as shown in Figure 10, an equivalent finite element model of the rotor with a curvic coupling is established based on the finite element method, as shown in Figure 11. CC_1, CC_2, CC_3 and CC_4 are 4 curvic couplings in different positions of the rotor, and their Young's modulus are the equivalent modulus which are calculated considering the influence of the bending moment on the contact stiffness. And the bending moment can be calculated by the unbalance mass, the rotational speed and the distance from the position of the unbalance mass to the position of curvic couplings.

FIGURE 10. The physical model of rotor with a curvic coupling.

The critical speeds of the rotor with the unbalance mass 40 g under different preload forces shown in Table 3 are calculated, the simulation results are shown in Figure 12.

In Figure 12, the solid line represents the first three critical speeds of the rotor in the forward whirling, and the dashed line represents the first three critical speeds of the rotor in the backward whirling. The specific values of the first three critical speeds of the rotor under different pre-tension forces can be found in Table 4.

According to Figure 12 and Table 4, it can be observed that with an increase in preload force, the contact stiffness of the curvic coupling increases, and the first three critical speeds of the rotor the curvic coupling rise. The first critical speed of the rotor is least affected by the preload force, while the third critical speed of the rotor is most affected by the preload force.

Comparative analysis of the rotor's first three critical speeds considering the influence of bending vibration on the contact stiffness of the curvic coupling and the rotor's first three critical speeds neglecting the influence of bending vibration on the contact stiffness of curvic coupling. The results are shown in Figure 13.

In Figure 13, K_{n1} is the contact stiffness considering the influence of bending vibration, K_{n2} is the contact stiffness not considering the influence of bending vibration.

According to Figure 13, it can be seen that bending vibration will reduce the stiffness of the rotor with curvic coupling, thereby affecting the first three critical speeds of the rotor. Since the first two critical speeds of the rotor are low, the bending moment caused by the unbalance mass is less than 10 N·m, the change in the contact stiffness is little.

However, at the third critical speed of the rotor, the bending moment caused by unbalance is greater than 500 N·m,

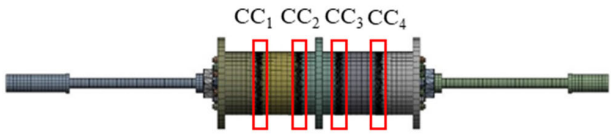

FIGURE 11. The finite element model of rotor system of rotor with a curvic coupling.

TABLE 2. Structural parameters of the rotor.

Name	Material	Density	Young's modulus	Poisson's ratio
Shaft	40CrA	7900 kg/m^3	211 Gpa	0.31
Disk	45 steel	7850 kg/m^3	210 Gpa	0.3
Nut	45 steel	7850 kg/m^3	210 Gpa	0.3
Rod	45 steel	7850 kg/m^3	210 Gpa	0.3

TABLE 3. Parameters of the preload force on the curvic coupling.

Preload force of each rod	Number of rods	Total preload force
1.50 kN	8	12 kN
5.00 kN	8	40 kN
7.50 kN	8	60 kN

the contact stiffness has significantly decreased. Therefore, the first two critical speeds of the rotors remain basically unchanged, while the third stage critical speed shows a noticeable change.

In Figure 14, the solid line represents the first three critical speeds of the rotor with the unbalance mass 40 g, and the dash-dot line represents the first three critical speeds of the rotor with the unbalance mass 20 g, and the dashed line represents the first three critical speeds of the rotor with the unbalance mass 0 g.

According to Figure 14, it can be observed that with an increase in the unbalance mass, the contact stiffness of the curvic coupling and the first three critical speeds of the rotor the curvic coupling decrease. The first two critical speed of the rotor is least affected by the unbalance mass, because the bending moment in the first two critical speed that is excited by the unbalance mass is less than 200 N·m and the stiffness loss caused by the bending moment can be ignored, which is shown in Figure 9. The third critical speed of the rotor is most affected by the preload force, because the bending moment in the third critical speed that is more than 500 N·m and the stiffness loss caused by the bending moment is significant, which is shown in Figure 9.

B. EXPERIMENTAL VALIDATION

The vibration characteristics of the rotors system with a curvic coupling under different preload forces using is studied by the rotor speed-up test. The test bench is shown in Figure 15, consisting of the non-continuous rotor, the support system, the power system, the data collection and analysis system.

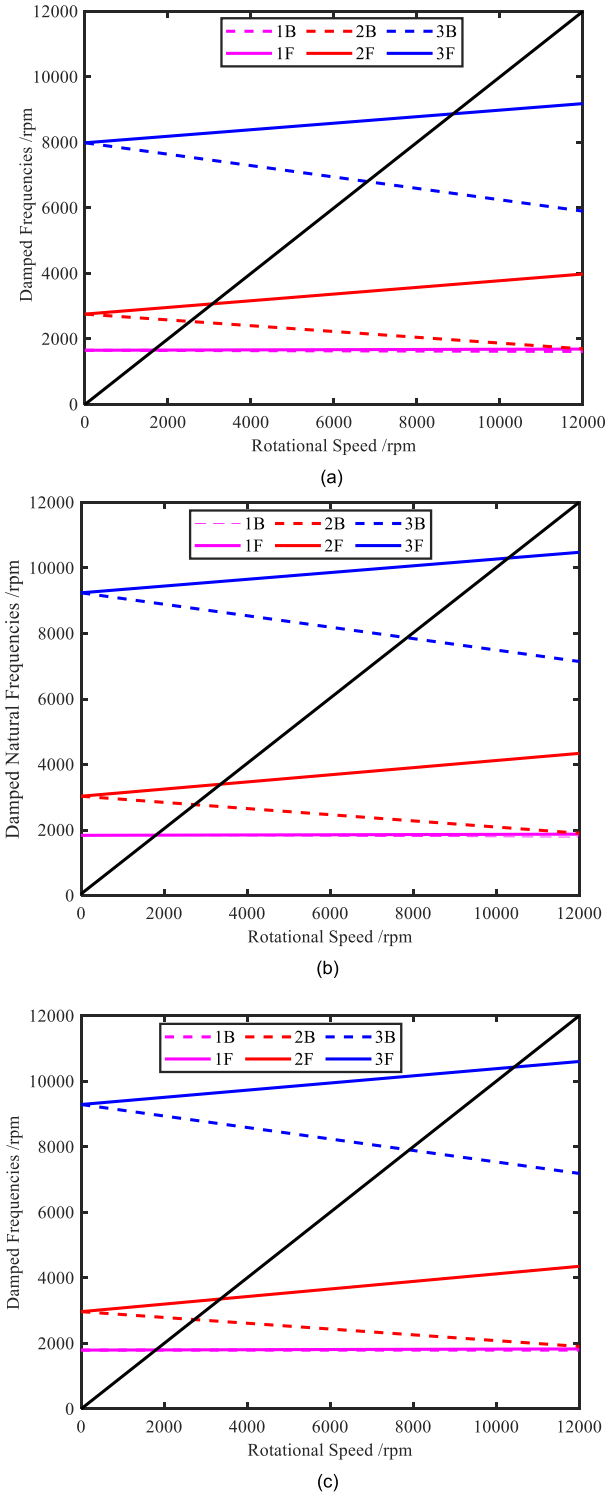

FIGURE 12. Campbell diagrams for the first three modes of the rotor under different preload forces. (a) Fp=12 kN, the first three modes of the rotor. (b) Fp=40 kN, the first three modes of the rotor. (c) Fp=60 kN, the first three modes of the rotor.

The non-continuous rotor is the rotor with a curvic coupling fastened by the rod, and the support system includes bearings and the elastic support, the power system provides

TABLE 4. Structural parameters of the rotor.

Preload force	First critical speed	Second critical speed	Third critical speed
12kN	1694rpm	3094rpm	9041rpm
40kN	1822rpm	3484rpm	10390rpm
60kN	1794rpm	3464rpm	10774rpm

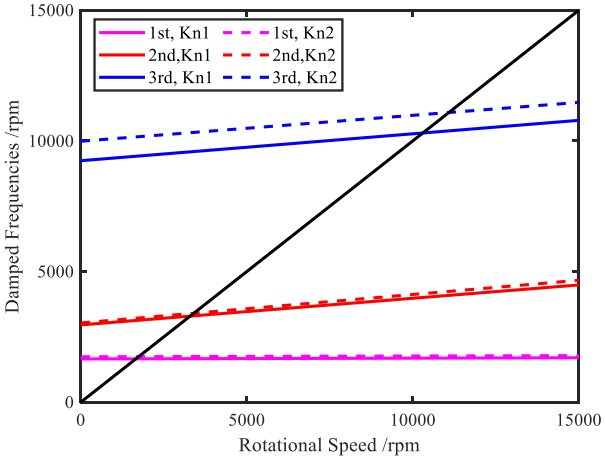

FIGURE 13. Fp=40 kN, the first three modes of the rotor with the different contact stiffness.

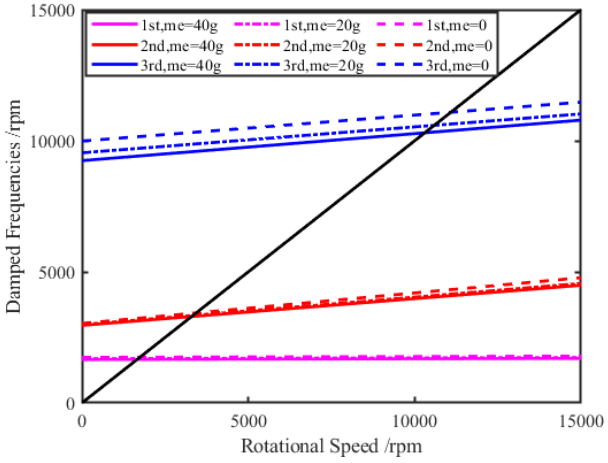

FIGURE 14. Fp=40 kN, the first three modes of the rotor with the different unbalance mass.

the rotational speed to the rotor, and the data collection and analysis system is used to record and analyze the rotor's vibration data.

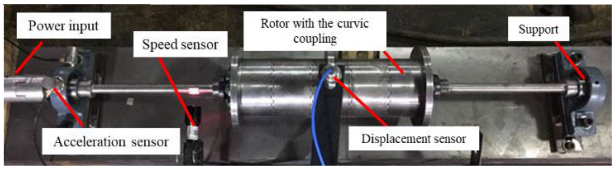

FIGURE 15. Fp=40 kN, the first three modes of the rotor with the different contact stiffness.

The critical speed and vibration response of the rotor are measured, the test operations are as follows:

Step (1). Apply the preload force 12 kN to the rotor with a curvic coupling, then install the rotor onto the test bench, and use the three-point dynamic balancing method to control the unbalance mass of the rotor, ensuring that the unbalance mass is 40g and the direction of the unbalance mass remains constant.

Step (2). Gradually increase the speed of the rotor and measure the vibration data of the rotor system in real-time, and process the collected data using dynamic testing analysis software to obtain the first two critical speeds and vibration responses of the test rotor.

Step (3). Change the preload force to 40 kN, and repeat the operations which are show in step 1 and step 2.

Step (4). Change the preload force to 60 kN, and repeat the operations which are show in Step (1) and Step (2).

The first two critical speeds and vibration responses of the rotor under different preload forces tested in the rotor speed-up test are shown in Figure 15.

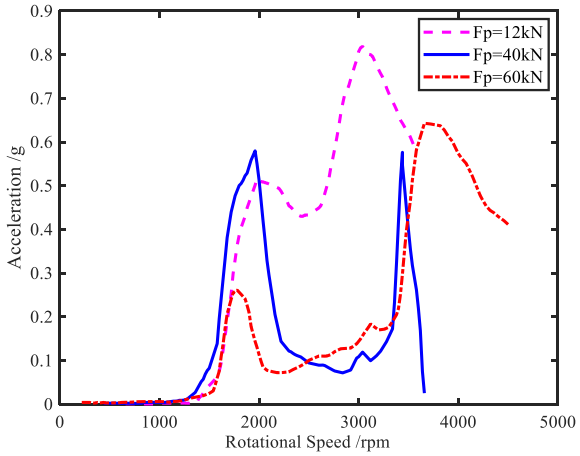

FIGURE 16. The first two critical speeds and vibration responses of the rotor under different preload forces (F_P = 12 kN, F_P = 40 kN and F_P = 60 kN).

In Figure 16, the red line represents the first two critical speeds and vibration response of the rotor under the preload forces 12 kN, the blue line represents the first two critical speeds and vibration response of the rotor under the preload forces 40 kN, and the purple line represents the first two critical speeds and vibration response of the rotor under the preload forces 60 kN.

Based on the experimental results, it can be observed that the first critical speed of the rotor is minimally affected by changes in preload force, while the second critical speed of the rotor is significantly affected. When the preload force increases, the second critical speed of the rotor also increases. The preload force is inversely proportional to the vibration response of the rotor. The greater the pre-tensioning force, the smaller the vibration response of the rotor.

The comparative analysis of the test results and simulation results is shown in Table 5.

TABLE 5. The first two critical speeds of the rotor under different preload forces.

Name	Preload force	Experiment	Simulation	Relative error
1st critical speed	12 kN	1976 rpm	1694 rpm	14.3%
1st critical speed	40 kN	1969 rpm	1822 rpm	7.5%
1st critical speed	60 kN	1780 rpm	1794 rpm	7.8%
2nd critical speed	12 kN	3039 rpm	3094 rpm	1.8%
2nd critical speed	40 kN	3440 rpm	3408 rpm	0.9%
2nd critical speed	60 kN	3664 rpm	3464 rpm	5.4%

The relative error of the experimental results compared to the simulation results for the second critical speed does not exceed 5.4%, the relative error is small. However, the relative error for the first critical speed is high, there is a maximum value 14.3%.

The reason for the large error of 1st critical speed is that the vibration mode corresponding to the first critical speed is mainly determined by the axial stiffness affected by the installation process of the experimental rotor system, such as the interaction between the rotor and the bearing and the connection between the rotor and the power machinery. During the experiment, the adjustment of the preload force should be changed three times. Due to design flaws in the rotor test bench and installation processes, there was a significant deviation in the axial stiffness of the rotor systems after changing the rotor's pre-tightening force.

On the other hand, the vibration mode corresponding to the second critical speed is mainly determined by factors such as structural dimensions, material properties, and preload force affecting the contact stiffness. The above factors are not affected by the installation technology and not changed during the process of adjusting the preload. The large error of 2nd critical speed can proves the correctness of the analytical model.

Therefore, the deviation in rotor structural stiffness after changing the rotor's preload force is relatively small. The comparison between the second critical speed of the simulation and the second critical speed of experimental indicates the correctness and effectiveness of the simulation model.

The experimental results validate the accuracy of the simulation analysis results in this paper, thereby indicating the reliability of the law of the contact stiffness of curvic coupling under bending vibration and the analysis results of the rotor's vibration characteristics in this paper.

VI. CONCLUSION

(1) This article analyzes the influence of bending vibration on the curvic coupling under the working conditions of the rotor. Based on the theory of elastic-plastic contact and Hertz contact, a three-dimensional contact stiffness model of considering the curvic coupling under the bending vibration is proposed. Subsequently, the finite

element model of the rotor with a curvic coupling is established based on the physical model of the experimental rotor.

(2) Based on the established model of contact stiffness of the curvic coupling, the influence of bending moment on the stiffness loss of the contact surface in the curvic coupling is investigated. The bending moment causes the contact stiffness of one half of the surface to increase and the contact stiffness of the other half to decreases. When the bending moment is small, the increase and decrease in contact stiffness are similar. However, when the bending moment is large, the increase in contact stiffness is significantly smaller than the decrease. The maximum bending moment varies with the position of the tooth surface. The maximum bending moment that prevents tooth separation should be less than 1.74% of the preload force.

(3) Based on the established model of contact stiffness of the curvic coupling, the influence of bending moment on the stiffness loss of the curvic coupling under the bending vibration is studied. The preload force affects the contact stiffness of the curvic coupling, when the bending moment is the same, the greater the preload force is, the greater the contact stiffness is, and the smaller the decrease in the contact stiffness caused by the bending moment is. The bending moment can weaken the contact stiffness of the curvic coupling, when the preload force is the same, the larger the bending moment, the smaller the contact stiffness, the bigger the decrease in the contact stiffness caused by the bending moment is.

(4) Based on the established finite element model of the rotor, the influence of the contact stiffness considering the effect of bending vibration on the dynamic characteristics of the rotor is analyzed. With an increase in preload force, the contact stiffness of the curvic coupling increases, and the first three critical speeds of the rotor the curvic coupling rise. The bending moment caused by the unbalance mass during bending vibration can affect the contact stiffness of the curvic coupling, therefor results in a decrease in the first three critical speeds of the rotor. Because the bending moment is directly determined by the square of the rotational speed, the first two critical speeds of the rotors remain basically unchanged, and the third critical speed has the most significant decrease.

REFERENCES

[1] J. Jam, F. Meisami, and N. Nia, "Vibration analysis of tie-rod/tie bolt rotors using FEM," *Int. J. Eng. Sci.*, vol. 3, no. 10, pp. 7292–7300, Oct. 2011.

[2] K. Xia, Y. Sun, F. Zhang, J. Guo, and L. Yu, "Impact of synchronous generator transient on gas turbine rotor," *Int. J. Appl. Electromagn. Mech.*, vol. 52, nos. 1–2, pp. 281–288, Dec. 2016.

[3] M. Zhuo, L. H. Yang, and L. Yu, "Contact stiffness calculation and effects on rotordynamic of rod fastened rotor," presented at the Mech. Solids, Struct. Fluids; NDE, Diagnosis, Prognosis, vol. 9, Phoenix, AZ, USA, Nov. 2016.

[4] K. Xia, Y. Sun, D. Hong, J. Guo, and X. Kang, "Effects of contact interfaces on rotor dynamic characteristics of heavy-duty gas turbine generator set," presented at the IEEE Int. Conf. Mechatronics Autom., Haerbin, China, Aug. 2016.

[5] Z. Rao, S. Xia, and G. Wang, "A study on rough plane contact stiffness," *J. Mech. Strength*, vol. 16, no. 2, pp. 72–75, Jun. 1994.

[6] Y. Zhang, Z. Du, L. Shi, and S. Liu, "Determination of contact stiffness of rod-fastened rotors based on modal test and finite element analysis," *J. Eng. Gas Turbines Power*, vol. 132, no. 9, Sep. 2010, Art. no. 094501.

[7] L. Shi and Y. Zhang, "Model test and analysis of gas turbine rotor," *Gas Turbine Technol.*, vol. 20, no. 4, pp. 47–49, Dec. 2007.

[8] L. Shi and Y. Zhang, "The measurement and calculation analysis of natural frequencies for rod fastening xiangtan," presented at the ROTDYN, vol. 27, Xiangtan, China, Jun. 2008.

[9] Q. Yuan, R. Gao, Z. Feng, and J. Wang, "Analysis of dynamic characteristics of gas turbine rotor considering contact effects and pre-tightening force," in *Proc. ASME Turbo Expo, Power Land, Sea, Air*, vol. 5, Berlin, Germany, Jun. 2008, pp. 983–988.

[10] Q. Yuan, J. Gao, and P. Li, "Nonlinear dynamics of the rod-fastened Jeffcott rotor," *J. Vibrat. Acoust.*, vol. 136, no. 2, Apr. 2014, Art. no. 021011.

[11] J. Gao, Q. Yuan, P. Li, Z. Feng, H. Zhang, and Z. Lv, "Effects of bending moments and pretightening forces on the flexural stiffness of contact interfaces in rod-fastened rotors," *J. Eng. Gas Turbines Power*, vol. 134, no. 10, Oct. 2012, Art. no. 102503.

[12] Y. Ma, Y. Y. Ni, X. Q. Chen, W. Q. Deng, and H. Yang, "Bending stiffness loss of rod-rabbet joints and its effect on vibration response of rotor systems," *Acta Aeronautica ET Astronautica Sinica*, vol. 42, no. 3, Mar. 2021, Art. no. 223861.

[13] H. Liu, J. Hong, and D. Zhang, "Bending and vibration of a discontinuous beam with a curvic coupling under different axial forces," *Frontiers Mech. Eng.*, vol. 15, no. 3, pp. 417–429, Sep. 2020.

[14] S. Yuan, "Dynamic characteristics and dynamic stress distribution of circvic couplings," in *Structure and Strength of Curvic Couplings*. Beijing, China: China Petrochemical Press, 2022, ch 5, pp. 103–135.

[15] R. Zhao, Y. Jiao, Z. Chen, Z. Li, and X. Qu, "Nonlinear analysis of a dual-disk rotor system considering elastoplastic contact," *Int. J. Non-Linear Mech.*, vol. 141, May 2022, Art. no. 103925.

XING HENG was born in Zhumadian, Henan, China, in 1992. He received the bachelor's degree in engineering from Wuhan University of Technology and the master's degree in engineering from Guangxi University. He is currently pursuing the Ph.D. degree with Central South University.

From 2016 to 2019, he was engaged in research on the fatigue and vibration characteristics of hydro turbines. Since 2019, he has been mainly focuses on research in rotor dynamics, and rotor vibration characteristics the design of rotor.

AILUN WANG was born in Changsha, Hunan, China, in 1959.

He is currently a Professor with the School of Mechanical and Electrical Engineering, Central South University. He has completed research work on the design, vibration analysis, vibration fault analysis, and strength analysis of gas turbines and aero-engine rotors. He has published two monographs and more than 80 SCI/EI articles. His research interests include mechanical system structural design, structural dynamics, system dynamics, large gas and steam turbines, and aircraft engine rotor dynamics.